INTERNATIONAL JOURNAL FOR NUMERICAL METHODS IN FLUIDS
Int. J. Numer. Meth. Fluids 2005; **49**:489–519
Published online 14 June 2005 in Wiley InterScience (www.interscience.wiley.com). DOI: 10.1002/fld.1002

Large eddy simulation of turbulent channel flow using an algebraic model

S. Bhushan*,† and Z. U. A. Warsi‡

Department of Aerospace Engineering, Mississippi State University, Starkville, Mississippi, MS 39762, U.S.A.

SUMMARY

In this paper an algebraic model from the constitutive equations of the subgrid stresses has been developed. This model has an additional term in comparison with the mixed model, which represents the backscatter of energy explicitly. The proposed model thus provides independent modelling of the different energy transfer mechanisms, thereby capturing the effect of subgrid scales more accurately. The model is also found to depict the flow anisotropy better than the linear and mixed models. The energy transfer capability of the model is analysed for the isotropic decay and the forced isotropic turbulence. The turbulent plane channel flow simulation is performed over three Reynolds numbers, $Re_\tau = 180$, 395 and 590, and the results are compared with that of the dynamic model, Smagorinsky model, and the DNS data. Both the algebraic and dynamic models are in good agreement with the DNS data for the mean flow quantities. However, the algebraic model is found to be more accurate for the turbulence intensities and the higher-order statistics. The capability of the algebraic model to represent backscatter is also demonstrated. Copyright © 2005 John Wiley & Sons, Ltd.

KEY WORDS: LES; algebraic model; turbulent channel flow

1. INTRODUCTION

The governing equations for large eddy simulation (LES) are obtained by filtering the Navier–Stokes equations. The filtering operation is defined by the convolution ($*$) of the variables of interest with a filter function, $G(\mathbf{x})$, of suitable width (Δ).

$$\hat{\mathbf{u}} = G(\mathbf{x}) * \mathbf{u} \tag{1}$$

*Correspondence to: Shanti Bhushan, SimCenter, Engineering Research Center, P.O. Box 9627, Starkville, MS 39762, U.S.A.
†E-mail: shanti@erc.msstate.edu
‡E-mail: warsi@ae.msstate.edu

Received 30 October 2004
Revised 12 April 2005
Accepted 23 April 2005

Further, assuming that the filtering and differentiation commute, the evolution of the resolved scales of motion for an incompressible flow are obtained as

$$\begin{aligned} \operatorname{div} \hat{\mathbf{u}} &= 0 \\ \frac{\partial \hat{\mathbf{u}}}{\partial t} + (\hat{\mathbf{u}} \cdot \operatorname{grad})\hat{\mathbf{u}} &= -\operatorname{grad} \hat{p} + \nu \operatorname{div}(\operatorname{grad} \hat{\mathbf{u}}) - \operatorname{div}(\boldsymbol{\tau}) \end{aligned} \tag{2}$$

where $\boldsymbol{\tau} = \widehat{\mathbf{uu}} - \hat{\mathbf{u}}\hat{\mathbf{u}}$ is the subgrid stress (SGS) tensor which is to be modelled. It has been identified that the main effect of the subgrid scales is to drain energy from the resolved scales of motion, but transfer occurs bi-directionally leading to both forward scatter and backscatter [1, 2] of energy. Hence, a successful closure of Equations (2) requires a SGS model which can represent these energy transfers accurately [3]. The most commonly used approach for modelling the stresses are the eddy viscosity linear model, as proposed by Smagorinsky (SM). Introduction of dynamic model (DSM) coefficient evaluation [4] technique improves the ability of the linear model to predict mean flow quantities vastly as it estimates the energy dissipation accurately [5]. Dynamic modelling thus accounts for backscatter of energy in an averaged sense [6]. However, studies [7] have shown that the nonlinearity has to be introduced to capture the backscatter effects, which is the foremost drawback of such models. There has been continuous efforts since, to model the backscatter mechanism independently rather than in an averaged sense [8, 9]. The stochastic model is one such approach [10, 11] and provides good results in specific cases. But, the universality of the approach is doubtful [12], as they cannot account for the deterministic structure of backscatter transfers [13].

The models based on the approximation of the total velocity field ($\mathbf{u}$) from the resolved velocity field ($\hat{\mathbf{u}}$), thereby computing the stresses directly from definition [14], are of growing interest in the LES community. This approach is inspired from the scale-similarity models of Bardina (cf. Reference [5]), where the total velocity was simply approximated as the resolved scale velocity. The scale-similarity approach has been further extended, using an explicit secondary filtering, based on the assumption that subgrid scales copy the scales (usually an octave) above. The secondary filtering can subsequently be avoided by Taylor's series expansion of such models, leading to a gradient model [15, 16]. However, the total velocity can be obtained directly by inverting the filtering operation (i.e. deconvolution), Equation (1) [14]. As the leading term of the SGS on deconvolution (usually retained [17]) is same as that of the gradient model [18], it can be concluded that above-mentioned class of models (although varying in details) have close ties [14]. Thus the drawbacks of the deconvolution methods can be associated with the scale-similarity and gradient models.

As is evident the deconvolution requires a non-zero filter transfer function, thus Gaussian filters are commonly used. Application of such smooth filters attenuates the effect of the small scales, but the resolved scale motion has a wide spectral realization. The exact computation of the SGSs through deconvolution requires information of the resolved scales of the order of DNS resolution. This is the reason for their high correlation in *a priori* analysis. However, in *a posteriori* simulation they are not sufficiently dissipative [14]. This aspect of the model can be analysed assuming that the numerical grids lead to a sharp spectral cut-off [19], thereby separating the flow variables into filtered ($\bar{\mathbf{u}}$) and unresolved ($\mathbf{u}''$) quantities. The solution of the equations of motion provides information for the filtered-resolved quantities ($\tilde{\mathbf{u}} \sim \hat{\bar{\mathbf{u}}}$) and the unknown stress terms are

$$\boldsymbol{\tau} = \widehat{\bar{\mathbf{u}}\bar{\mathbf{u}}} - \hat{\bar{\mathbf{u}}}\hat{\bar{\mathbf{u}}} \tag{3}$$

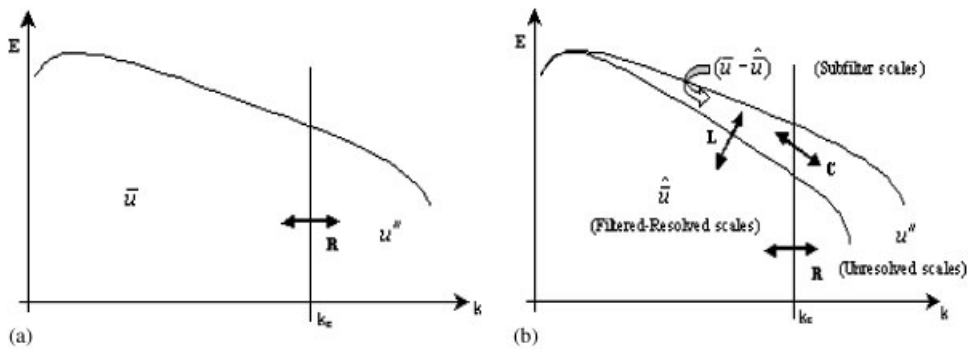

Figure 1. Graphical representation of the interaction between resolved and subgrid scales namely Leonard's (**L**), cross (**C**) and Reynold's (**R**) components as defined in Equation (13), where symbol '$\longleftrightarrow$' represents energy transfer across scales of motion: (a) sharp cut-off filter; and (b) smooth filter.

Decomposing the total velocity field as the filtered and unresolved components in Equation (3) along with the identity that the sharp cut-off filtering satisfies Reynold's assumption yields,

$$\boldsymbol{\tau} = \widehat{\bar{\mathbf{u}}\,\bar{\mathbf{u}}} - \hat{\bar{\mathbf{u}}}\hat{\bar{\mathbf{u}}} + \widehat{\mathbf{u}''\mathbf{u}''} \tag{4}$$

The first term in the decomposition is referred to as the subfilter stress (SFS) [19], and represents the interaction **L** in Figure 1. The deconvolution method can represent these stresses accurately, and the dominant term of the Taylor's series expansion of SFS may be assumed to be its representative model. That is,

$$\widehat{\bar{\mathbf{u}}\,\bar{\mathbf{u}}} - \hat{\bar{\mathbf{u}}}\hat{\bar{\mathbf{u}}} = \alpha_1 \Delta^2 (\text{grad } \tilde{\mathbf{u}} \cdot [\text{grad } \tilde{\mathbf{u}}]^{\mathrm{T}}) \tag{5}$$

The additional correlation appearing in Equation (4) represents the effect of unresolved scales and corresponds to interaction of type $\mathbf{R} + \mathbf{C}$ in Figure 1. Not much attention has been paid to the modelling of this term [3] and are commonly modelled as purely dissipative eddy viscosity term [16, 19], leading to a mixed model (MM) [14, 20].

$$\boldsymbol{\tau} = \tfrac{2}{3} K_{\text{sgs}} \mathbf{I} - 2C_{\text{s}}^2 \Delta^2 [2\tilde{\mathbf{D}} : \tilde{\mathbf{D}}]^{1/2} \tilde{\mathbf{D}} + \alpha_1 \Delta^2 [\text{grad } \tilde{\mathbf{u}} \cdot (\text{grad } \tilde{\mathbf{u}})^{\mathrm{T}} - \tfrac{1}{3} (\text{grad } \tilde{\mathbf{u}} : \text{grad } \tilde{\mathbf{u}}) \mathbf{I}] \tag{6}$$

where C_{s}^2 and α_1 are the unknown model coefficients, $\tilde{\mathbf{D}}$ is the rate-of-strain tensor and K_{sgs} is the subgrid scale kinetic energy. It has often been argued that the SFS (scale-similar) terms are responsible for the backscatter of energy [20], justifying the use of purely dissipative model for unresolved stresses. However, for the sharp spectral filter the SFS terms go to zero (as evident from Figure 1) and so does the backscatter of energy, which is not consistent with the DNS results [1]. Studies show that most of the backscatter is via the non-local interaction represented by unresolved scales in Equation (4) [12, 21]. Hence, the modelling of these correlations as purely dissipative (eddy viscosity) term does not provide proper modelling of backscatter.

The purpose of this paper is to propose an algebraic model (AM) obtained directly from the constitutive equations of the SGSs, which is discussed in the following section. The AM

provides an additional term over the mixed model, which models the forward and backscatter phenomenon via the unresolved scale correlation explicitly. The unknown model coefficients are computed in the framework of isotropic turbulence in Section 3, to provide the appropriate amount of energy dissipation. The capability of the model to predict stress anisotropy is tested in Section 4, and its energy transfer capability assessed in Section 5 for isotropic turbulence simulations. The model performance is also compared with SM and MM. In Section 6 turbulent channel flow simulations have been performed over the Reynolds numbers $Re_\tau = 180$, 395 and 590. The model performance is compared with the SM, DSM, and the DNS [22] results. Finally, some conclusions are drawn in Section 7.

2. ALGEBRAIC MODEL

The transport equation of SGSs (3) can be obtained from the Navier–Stokes equations, which in component form is written as

$$\begin{aligned}\frac{\tilde{D}}{Dt}\tau_{ik} = &-\left[\frac{\partial \widetilde{u_i u_j u_k}}{\partial x_j} - \frac{\partial \tilde{u}_i \tau_{kj}}{\partial x_j} - \frac{\partial \tilde{u}_j \tau_{ik}}{\partial x_j} - \frac{\partial \tilde{u}_k \tau_{ij}}{\partial x_j} - \frac{\partial \tilde{u}_i \tilde{u}_j \tilde{u}_k}{\partial x_j}\right] \\ &-\frac{1}{\rho}\left[\frac{\partial \widetilde{pu_i}\delta_{kj}}{\partial x_j} - \frac{\partial \tilde{p}\tilde{u}_i\delta_{kj}}{\partial x_j} + \frac{\partial \widetilde{pu_k}\delta_{ij}}{\partial x_j} - \frac{\partial \tilde{p}\tilde{u}_k\delta_{ij}}{\partial x_j}\right] + \frac{1}{\rho}\left[p\widetilde{\frac{\partial u_k}{\partial x_i}} - \tilde{p}\frac{\partial \tilde{u}_k}{\partial x_i} + p\widetilde{\frac{\partial u_i}{\partial x_k}} - \tilde{p}\frac{\partial \tilde{u}_i}{\partial x_k}\right] \\ &+ \nu\nabla^2\tau_{ik} - 2\nu\left[\widetilde{\frac{\partial u_i}{\partial x_l}\frac{\partial u_k}{\partial x_l}} - \frac{\partial \tilde{u}_i}{\partial x_l}\frac{\partial \tilde{u}_k}{\partial x_l}\right] - \left[\tau_{ij}\frac{\partial \tilde{u}_k}{\partial x_j} + \tau_{kj}\frac{\partial \tilde{u}_i}{\partial x_j}\right] \end{aligned} \tag{7}$$

where the substantive derivative is

$$\frac{\tilde{D}}{Dt} = \frac{\partial}{\partial t} + \tilde{u}_k\frac{\partial}{\partial x_k}$$

Introducing a set of generalized central moments for subgrid scales [23]

$$\lambda(u_i, u_j) = \widetilde{u_i u_j} - \tilde{u}_i\tilde{u}_j$$

$$\lambda(u_i, u_j, u_k) = \widetilde{u_i u_j u_k} - \tilde{u}_i\lambda(u_j, u_k) - \tilde{u}_j\lambda(u_k, u_i) - \tilde{u}_k\lambda(u_i, u_j) - \tilde{u}_i\tilde{u}_j\tilde{u}_k$$

the terms on right of Equation (7) can be expressed in terms of diffusion, dissipation, production and pressure–strain correlation [5, 24].

$$P_{ij} = -\left[\tau_{ik}\frac{\partial \tilde{u}_j}{\partial x_k} + \tau_{kj}\frac{\partial \tilde{u}_i}{\partial x_k}\right]$$

$$Q_{ij} = \lambda\left(\frac{p}{\rho}, \frac{\partial u_i}{\partial x_j} + \frac{\partial u_j}{\partial x_i}\right)$$

$$F_{ij} = -\frac{\partial}{\partial x_k}\left[\lambda(u_i, u_j, u_k) + \lambda\left(\frac{p}{\rho}, u_i\delta_{kj} + u_j\delta_{ik}\right)\right]$$

$$\varepsilon_{ij} = 2\nu\lambda\left(\frac{\partial u_i}{\partial x_k}, \frac{\partial u_j}{\partial x_k}\right)$$

The subgrid scale kinetic energy, $K_{\text{sgs}} = \frac{1}{2}(\widetilde{u_i u_i} - \tilde{u}_i \tilde{u}_i)$, equation is obtained from the summation of Equation (7) as

$$\frac{\partial K_{\text{sgs}}}{\partial t} + \tilde{u}_k \frac{\partial K_{\text{sgs}}}{\partial x_k} = P + D - \varepsilon + \nu \nabla^2 K_{\text{sgs}} \tag{8}$$

where $P = \frac{1}{2}P_{ii}$; $D = \frac{1}{2}F_{ii}$; $\varepsilon = \frac{1}{2}\varepsilon_{ii}$ and $Q_{ii} = 0$ (from the continuity equation). As the SGSs have been cast in the framework of RANS (Reynold's averaged Navier–Stokes) stresses [25], similar modelling procedure can be applied. However, it must be noted that the correlations defined above have been expressed as generalized subgrid moments, which contain the physical aspect of the SGS. The modelling of these correlations, although analogous to RANS stresses, must be understood in terms of subgrid moments. The salient points in the modelling of these correlations are discussed in Appendix A (also refer to Reference [25]). The algebraic stress closure for the SGS, where $T_{ij} = \tau_{ij}/K_{\text{sgs}}$, are

$$T_{ij}(P - \varepsilon) = P_{ij} + Q_{ij} - \varepsilon_{ij} \tag{9}$$

2.1. Deductive iteration

On introducing the quantity

$$M_{ij} = \frac{K_{\text{sgs}}}{\varepsilon} \frac{\partial \tilde{u}_i}{\partial x_j}$$

in the modelling of P_{ij} and Q_{ij} (cf. Appendix) and following Warsi [25] a deductive iterative scheme for solving Equation (9) is formulated as follows:

$$\begin{aligned} a_0 T_{ij}^{(n+1)} = {} & T_{ij}^{(n)} T_{kl}^{(n)} M_{kl} + \tfrac{2}{3}\delta_{ij}[a_0 + (\gamma_0 - 1 - \beta) T_{kl}^{(n)} M_{kl}] \\ & - \gamma[M_{ij} + M_{ji}] - \gamma_0[T_{ik}^{(n)} M_{jk} + T_{jk}^{(n)} M_{ik}] + \beta[T_{ik}^{(n)} M_{kj} + T_{jk}^{(n)} M_{ki}] \end{aligned} \tag{10}$$

For the zeroth-order approximation we assume isotropic form of the stress tensor ($\tau_{ij}^{(0)} = \frac{2}{3}K_{\text{sgs}}\delta_{ij}$). Upon substitution the first-order approximation is obtained as follows:

$$\tau_{ij}^{(1)} = \frac{2}{3}K_{\text{sgs}}\delta_{ij} - 2A\frac{K_{\text{sgs}}^2}{\varepsilon}\tilde{D}_{ij} \tag{11}$$

where $A = (\gamma + 2/3\gamma_0 - 2/3\beta)/a_0$. As evident, Equation (11) is the eddy viscosity model. The second-order approximation of the stress terms can be obtained similarly. Keeping the terms of interest and expressing turbulent kinetic energy and dissipation in terms of filter width (Δ) [24]. The algebraic stress model thus obtained is expressed in coordinate-invariant form as follows:

$$\begin{aligned} \boldsymbol{\tau} = {} & \tfrac{2}{3}K_{\text{sgs}}\mathbf{I} - 2C_s^2\Delta^2[2\tilde{\mathbf{D}} : \tilde{\mathbf{D}}]^{1/2}\tilde{\mathbf{D}} + \alpha_1\Delta^2[\text{grad}\ \tilde{\mathbf{u}} \cdot (\text{grad}\ \tilde{\mathbf{u}})^{\mathrm{T}} - \tfrac{1}{3}(\text{grad}\ \tilde{\mathbf{u}} : \text{grad}\ \tilde{\mathbf{u}})\mathbf{I}] \\ & - \alpha_2\Delta^2[(\text{grad}\ \tilde{\mathbf{u}})^{\mathrm{T}} \cdot \text{grad}\ \tilde{\mathbf{u}} - \tfrac{1}{3}(\text{grad}\ \tilde{\mathbf{u}} : \text{grad}\ \tilde{\mathbf{u}})\mathbf{I}] \end{aligned} \tag{12}$$

Comparing Equations (6) and (12), it is observed that AM provides an additional term over the mixed model. The role of the model terms in the energy transfer mechanism can be studied by the closure of SGSs with the rate-of-strain tensor in the canonical approach

(cf. Appendix B). The second term is purely dissipative in nature, whereas (for positive model coefficient) the fourth term provides backscatter of energy. Essentially, the eddy viscosity and backscatter terms in Equation (12) represent the unresolved stresses in Equation (4), as opposed to eddy viscosity in MM. Thus the AM provides a better modelling of the energy transfer mechanism. Similar terms were also obtained by Horiuti [26] and are present in LANS-α model [27], but their energy transfer capability were not explored. The evaluation of the unknown model coefficients, to produce appropriate amount of energy dissipation, is discussed below.

3. ENERGY TRANSFER

The decomposition of SGSs in Equation (4) as $\mathbf{L}, \mathbf{C}$ and $\mathbf{R}$ is now carried out as follows. Substituting $(\mathbf{u}'' = \mathbf{u}' + \tilde{\mathbf{u}} - \bar{\mathbf{u}})$ in Equation (4), the SGSs are partitioned as

$$\boldsymbol{\tau} = \underbrace{(\widetilde{\tilde{\mathbf{u}}\tilde{\mathbf{u}}} - \tilde{\bar{\mathbf{u}}}\,\tilde{\bar{\mathbf{u}}})}_{\mathbf{L}} + \underbrace{(\widetilde{\tilde{\mathbf{u}}\mathbf{u}'} - \tilde{\bar{\mathbf{u}}}\,\tilde{\mathbf{u}}') + (\widetilde{\mathbf{u}'\tilde{\mathbf{u}}} - \tilde{\mathbf{u}}'\,\tilde{\bar{\mathbf{u}}})}_{\mathbf{C}} + \underbrace{(\widetilde{\mathbf{u}'\mathbf{u}'} - \tilde{\mathbf{u}}'\,\tilde{\mathbf{u}}')}_{\mathbf{R}} \tag{13}$$

These stress terms can also be obtained directly by introducing the velocity decomposition $(\mathbf{u} = \tilde{\mathbf{u}} + \mathbf{u}')$ in Equation (3) (involves numerical filtering implicitly). These stress terms are Galilean invariant and are called the modified Leonard's, cross and Reynolds' stresses [23]. In this regard refer to Figure 1 [19]. The above decomposition of stresses helps to estimate the amount of energy transferred via different scale interactions. The analysis of these energy transfer processes can be accomplished either in physical space or in spectral space using the eddy damped quasi-normal Markovian (EDQNM) theory. The triad interaction $(\mathbf{k} = \mathbf{k}' + \mathbf{k}'')$ associated with these components are summarized as [2, 5]:

$$\begin{aligned}
&\grave{\mathbf{L}} : \mathbf{k} < \mathbf{k}_c, \quad \mathbf{k}' < \mathbf{k}_c, \quad \mathbf{k}'' < \mathbf{k}_c \\
&\grave{\mathbf{C}} : \mathbf{k} < \mathbf{k}_c, \quad \mathbf{k}_c < \max(\mathbf{k}', \mathbf{k}'') < 2\mathbf{k}_c, \quad \min(\mathbf{k}', \mathbf{k}'') < \mathbf{k}_c \\
&\grave{\mathbf{R}} : \mathbf{k} < \mathbf{k}_c, \quad \mathbf{k}' > \mathbf{k}_c, \quad \mathbf{k}'' > \mathbf{k}_c
\end{aligned} \tag{14}$$

where $\mathbf{k}_c$ is the LES cut-off wavenumber associated with numerical filtering, and $\grave{\mathbf{L}}$, $\grave{\mathbf{C}}$, $\grave{\mathbf{R}}$ are the respective Fourier transforms of $\mathbf{L}$, $\mathbf{C}$, and $\mathbf{R}$.

3.1. *Modified Leonard's term* (L)

This term is responsible for a substantial amount of dissipation [1, 15]. Leonard estimated the dissipation produced by the non-Galilean-invariant definition of this term using triple correlation tensor ($\tilde{T}_{ij,k} = \langle (\tilde{u}_i)_A (\tilde{u}_j)_A (\tilde{u}_k)_B \rangle$). Similar approach can be used to estimate the dissipation produced by modified Leonard's term defined in Equation (13). The rate of energy cascade due to this term is

$$\varepsilon_L = \left\langle \tilde{u}_i \frac{\partial \widetilde{\tilde{u}_i \tilde{u}_j}}{\partial x_j} \right\rangle - \left\langle \tilde{u}_i \frac{\partial \tilde{\bar{u}}_i \tilde{\bar{u}}_j}{\partial x_j} \right\rangle \tag{15}$$

The first term on the right is the same as computed in Leonard [15] whereas, the second term cannot be directly expressed in terms of $\tilde{T}_{ij,k}$. Applying Taylor's expansion on this term [28] we get

$$\left\langle \tilde{u}_i \frac{\partial \tilde{\tilde{u}}_i \tilde{\tilde{u}}_j}{\partial x_j} \right\rangle = \left\langle \tilde{u}_i \frac{\partial \tilde{u}_i \tilde{u}_j}{\partial x_j} \right\rangle + b \left[\left\langle \tilde{u}_i \frac{\partial}{\partial x_j} \left(\tilde{u}_j \frac{\partial^2 \tilde{u}_i}{\partial x_l \partial x_l} \right) \right\rangle + \left\langle \tilde{u}_i \frac{\partial}{\partial x_j} \left(\tilde{u}_i \frac{\partial^2 \tilde{u}_j}{\partial x_l \partial x_l} \right) \right\rangle \right] \tag{16}$$

where $b = \Delta^2/24$ is the second moment for the Gaussian filter. In Equation (16) the first term is zero because of the continuity equation [29] and the other terms can now be easily expressed in terms of $\tilde{T}_{ij,k}$. The net dissipation by the modified Leonard's term is thus obtained as [24]

$$\varepsilon_{\mathrm{L}} = -\tfrac{35}{24} K_{\mathrm{sgs}}^{3/2} K_0'''(0) \Delta^2 \approx 0.44\varepsilon \tag{17}$$

where $K_{\mathrm{sgs}}^{3/2} K_0'''(0) = \langle (\partial \tilde{u}_1/\partial x_1)^3 \rangle$ [29]. The modified Leonard's term can be identified with the SFS (scale-similarity model) and its Taylor's series expansion [28] yields the gradient model (Equation (5)). Closure of Equation (5) with the rate-of-strain tensor produces exactly the same amount of dissipation (ref. Appendix B) as above in (17). It must be noted that original calculations of Leonard [15] (based on non-Galilean invariant term) did not satisfy the dissipation criteria which was restored by using the second-order derivative [18] terms.

3.2. *Modified Reynolds' term* (**R**)

Information of the modified Reynolds' term cannot be obtained directly in physical space. But, in spectral space closed integrals are available for the *non-local expansion* involving triad interaction of References [12, 21]

$$\mathbf{k} \ll \mathbf{k}_{\mathrm{c}}, \quad \mathbf{k}' \sim \mathbf{k}'' > \mathbf{k}_{\mathrm{c}}$$

The above interaction is a component of modified Reynolds' stresses as evident from Equation (14). The EDQNM approximations of the forward ($F = c_{\mathrm{f}}\varepsilon$) and backscatter ($B = c_{\mathrm{b}}\varepsilon$) in this limiting case are [10, 24] such that

$$\int_0^{\mathbf{k}_{\mathrm{c}}} [F(\mathbf{k}) - B(\mathbf{k})] \, \mathrm{d}\mathbf{k} \approx 0.56\varepsilon \tag{18}$$

3.3. *Modified cross term* (**C**)

This term (from Equation (14)) corresponds to the *near-local expansion* which represents the interaction in the wavenumber range:

$$\mathbf{k} \sim \mathbf{k}_{\mathrm{c}}, \quad (\mathbf{k}' \text{ or } \mathbf{k}'') \sim \mathbf{k}_{\mathrm{c}} \quad \text{and} \quad (\mathbf{k}'' \text{ or } \mathbf{k}') \ll \mathbf{k}_{\mathrm{c}}$$

Unfortunately, no analytic integration can be performed for the above expansion [21], thus not much information can be drawn for the cross terms. However, a rough estimate of the net dissipation yields $\varepsilon_{\mathrm{C}} \approx 0$.

$$\varepsilon = \varepsilon_{\mathrm{L}} + \varepsilon_{\mathrm{C}} + \varepsilon_{\mathrm{R}}$$

$$[\approx 0.44\varepsilon] \quad [\approx 0] \quad [\approx 0.56\varepsilon]$$

The above estimate is in accordance with the numerical results [1, 30] which shows that the forward and backscatter via the cross term, diverge across the cut-off wavenumber but, cancel each other exactly. Although, cross stresses do not change the net energy of the system but, effects the evolution of resolved scale motion [10]. The modelling of these terms independently to reproduce the divergence effect cannot be achieved. However, the combined effect of modified Reynolds' and cross terms show a cusp near cut-off [30], leading to finite forward and backscatter transfers of energy. As *non-local expansion* is valid only in the limiting case the backscatter over the whole wavenumber range can be approximated by imposing local equilibrium [12]. The forward scatter can be modified similarly by imposing Equation (18) to obtain

$$c_f = 0.736 \quad \text{and} \quad c_b = 0.176 \tag{19}$$

The above energy transfer coefficients are identified with the combined effect of the modified Reynolds' and cross terms [8] and will be used in the model coefficient computation.

3.4. Model coefficients

To evaluate the model coefficients we identify the model terms in Equation (12) with different energy transfer mechanisms discussed above. The third term is the Taylor's expansion of modified Leonard's term and it produces exactly the same amount of dissipation (ref. discussion after Equation (17)). Thus α_1 can be obtained immediately. The second term is purely dissipative in nature and the model coefficient C_s^2 must account for the forward scatter of energy c_f whereas, α_2 must be evaluated to produce the estimated backscatter (c_b), approximated in Equation (19). The coefficients are computed in the framework of canonical case (ref. Appendix B) as presented in Table I. The model coefficients for the mixed model Equation (6) can also be computed following the above approach, where C_s^2 now account for the net energy transfer ($c_f - c_b$).

Table II presents the energy transfer by the model terms in *a posteriori* LES, discussed later in the paper. It can be observed that although the coefficients vary from the canonical

Table I. Model coefficients of the SGS models obtained from the canonical approach using the Gaussian filter.

	C_s^2	α_1	α_2
Smagorinsky model	0.0256	—	—
Mixed model	0.0162	$\frac{1}{12}$	—
Algebraic model	0.0213	$\frac{1}{12}$	0.03364

Table II. Energy transfer coefficients by the model terms in the homogeneous isotropic turbulence.

	c_f	c_L	c_b
Canonical case	0.736	0.44	0.176
Isotropic decaying	0.82	0.325	0.145
Forced isotropic	0.8	0.335	0.135

case (for which the model coefficients are calibrated), but are in acceptable limits. Overall, the model terms depict the energy transfer mechanism, that they were attributed to, satisfactorily. Thus the objective of developing a SGS model which can account for different energy transfer mechanism (independently) is fulfilled. In the following sections the performance of the AM is assessed by comparison with the existing models.

4. EFFECT OF NONLINEARITY

The principal axes of the stress tensor and the strain-rate tensor are not parallel for most flows [7] and is a familiar analysis tool in RANS modelling [25]. The same idea can be extended to the SGS modelling adopting a simplified picture according to which the turbulent subgrid scale field is locally subject to resolved strain or shear [8]. However, as the SGSs depend on the applied filter width the results cannot be compared with the experimental results (which are the Reynolds' stresses). However, the *a priori* analysis, for the rapid straining of turbulence [16], show that the anisotropic SGSs assume the same ratio as that of Reynolds stresses, over a wide range of filter width. Thus a SGS model should depict the same anisotropic stress ratio as that of the Reynolds' stresses [8, 31]. The simplest cases for which the normal anisotropic stresses show departure from the linearity are the *plane shear* and *plane strain* flows. For these cases the non-zero velocity gradient components are

$$\text{plane shear flow:} \quad \frac{\partial \tilde{u}_1}{\partial x_3} = C$$

$$\text{plane strain flow:} \quad \frac{\partial \tilde{u}_1}{\partial x_1} = C; \quad \frac{\partial \tilde{u}_2}{\partial x_2} = -C$$

Substituting these velocity gradient components in the SGS models Equation (12) with model coefficients in Table I, the anisotropic stress ratios obtained are presented in Table III (compared with experimental values of Tavoularis and Corrsin (1981) and Gence and Mathieu (1979) for *plane shear* and *strain* flows, respectively, see Reference [24] for related references). As is evident the SM fails to predict the stress anisotropy in both the cases. The MM shows some stress anisotropy, however, the best results are obtained for the AM. These results encourage the addition of the backscatter term over the MM.

Table III. Anisotropic stress ratio for homogeneous *plane shear* and *plane strain* flows.

$\sigma_{11}:\sigma_{22}:\sigma_{33}$	Plane shear	Plane strain
Experimental	0.2 : −0.06 : −0.14	0.23 : −0.16 : −0.07
Linear model		0.23 : −0.23 : 0.0
Mixed model	0.2 : −0.1 : −0.1	0.23 : −0.092 : −0.138
Algebraic model	0.2 : −0.05 : −0.15	0.23 : −0.155 : −0.075

5. ISOTROPIC TURBULENCE CASES

Numerical simulations has been performed for isotropic decaying and forced isotropic turbulence in a periodic cubic box of side 2π. The governing equations are solved using a pseudo-spectral code, where 3/2-rule is used to remove the aliasing error along homogeneous directions, and a second-order Runge–Kutta scheme for time evolution [32]. The initial velocity fields for these cases are generated following Rogallo [32]. For the decaying turbulence the energy spectrum is obtained from the experimental results of Comet-Bellot and Corrsin (CBC) (cf. Reference [32]) ($Re = 1346$), whereas for the forced turbulence case the Kolmogrov's $-5/3$ spectra is used. The mean velocities in these cases are taken to be zero, by specifying the velocity components for the wavenumber ($k = 0$) to be zero. Thus only the turbulent scales of motion are resolved in these cases. The initial random phases adjust themselves to physically acceptable values in the beginning of the simulation, leading to a transient period. The dynamic Smagorinsky model coefficient stabilize to $C = 0.03$ (for filter width ratio of 2) [32] at the end of the transient phase. Thus the results using SM were obtained using this constant value. For the MM and the AM filter width (Δ) is chosen such that $G(k_c) = 0.8$ [33] (the transfer function at cut-off where k_c is based on grid scale) as the model coefficients were obtained for the Gaussian filter. The simulations also help to assess the capability of AM terms in depicting the energy transfer mechanism, as shown in Table II.

5.1. Decaying turbulence

Isotropic decaying turbulence serves as an important benchmark for studying the energy transfer capability of the SGS model. Here, simulations have been performed for three different grid resolutions 32^3, 48^3 and 64^3. Figure 2 compares the evolution of the resolved scale kinetic energy for the three models considered. A simulation without any SGS model (NM) is also performed on 32^3 grid to emphasize on the contribution of these stress terms. NM case does not dissipate energy properly and leads to energy pile up across cut-off wavenumber. It can be observed that SM is more dissipative than the AM followed by the MM. More insight on this behaviour of the models can be obtained from the comparison of the energy spectrum, shown in Figure 3. The AM has more energy in the higher wavenumber range than the MM and the SM, thereby predicting more energy overall. This is due to the inclusion of the explicit backscatter term. AM predicts a wider inertial subrange than the other two models and thus captures the energy transfer better. The MM behaves more like AM and certainly provides improvement over SM. The transfer spectra of different terms of the AM (12) are presented in Figure 4. The eddy viscosity term dissipates energy from all resolved scales whereas, the Leonard's term dissipates more energy from intermediate wavenumber range. As is seen the energy input by the backscatter term is not localized to small wavenumbers but increases across cut-off wavenumber [30] thus, backscatter occurs in a realistic fashion.

5.2. Forced turbulence

The statistically stationary homogeneous turbulence, provides an ideal framework to study the capability of a turbulence model to predict the universal Kolmogrov's energy spectrum [11, 27]. The turbulence field is simulated by adding a forcing ($\mathbf{f}_k$) to the lower wavenumber

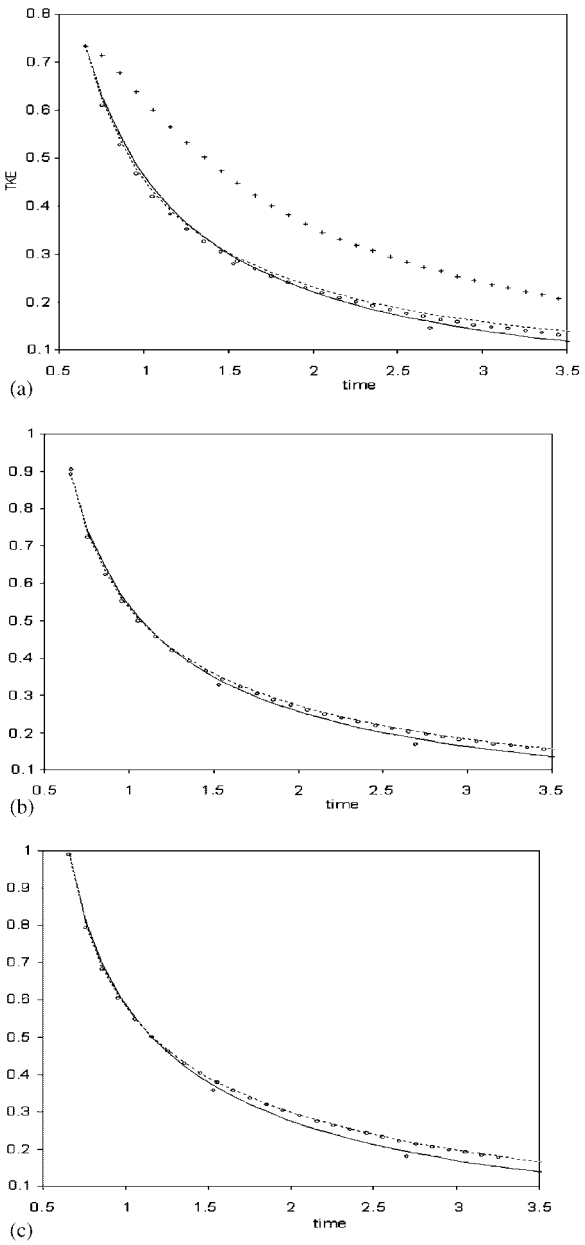

Figure 2. Resolved scale kinetic energy (TKE) evolution for: (a) 32^3 grid; (b) 48^3 grid; and (c) 64^3 grid cases using: ——: SM; - - - -: MM; ○ : AM; + : no model; ◇ : experimental [32].

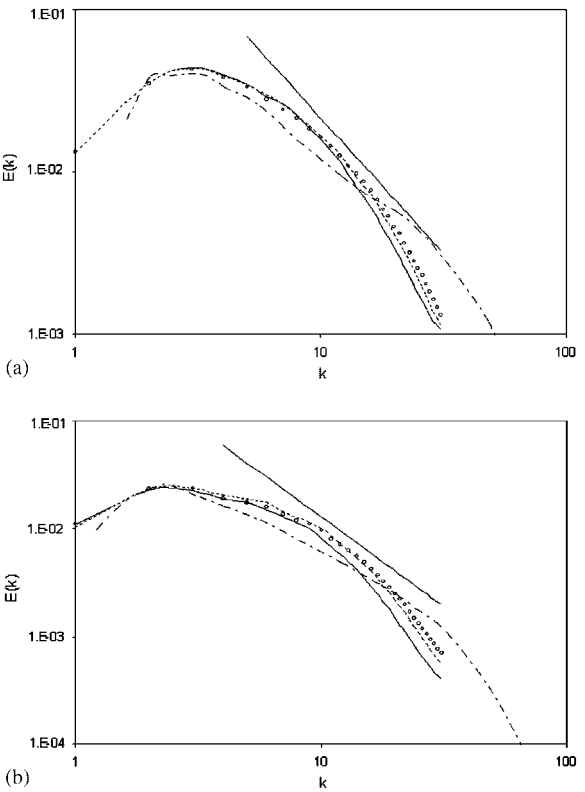

Figure 3. Energy spectra for 64^3 grid case at: (a) $t = 1.53$; and (b) $t = 2.7$ obtained from: ——: SM; - - - -: MM; ○: AM; —·—: experimental [32]; straight line: $k^{-5/3}$.

modes of Navier–Stokes equations defined as

$$\mathbf{f}_k = \frac{\varepsilon}{N} \frac{\mathbf{u}_k}{|\mathbf{u}_k|^2}$$

where ε is the energy injection rate and N is the number of Fourier modes in the shell $|\mathbf{k}| = k_0$ that are excited. For all the simulations presented here, $k_0 = 2$ is chosen. The simulations have been performed on three grid resolutions 32^3, 48^3 and 64^3 for infinite Reynolds number. Thus the energy transfer and dissipation occurs via the SGS terms only. On the coarse grid of 32^3 two energy injection rates $\varepsilon = 0.1$ and 0.2 have been considered, whereas other simulations are performed for $\varepsilon = 0.1$ only. Simulation on the fine grid 64^3 has been performed only using the AM. Figure 5 compares the Kolmogrov's constant, $C_k = E(k)\varepsilon^{-2/3}k^{5/3}$, predicted by the SGS models, where energy spectra is averaged over a sufficiently long period of time, after the statistical equilibrium, to obtain the mean values. The experimentally measured values of C_k are in the range 1.3–2.1 [10] in the inertial subrange. All the simulations show that C_k vary about 1.5, as observed by other authors [11]. The AM predicts flatter C_k profile followed by the SM and MM. The turbulent cascade develops independent of the amount of energy injected into the system as evident from the coarse grid simulation. All the

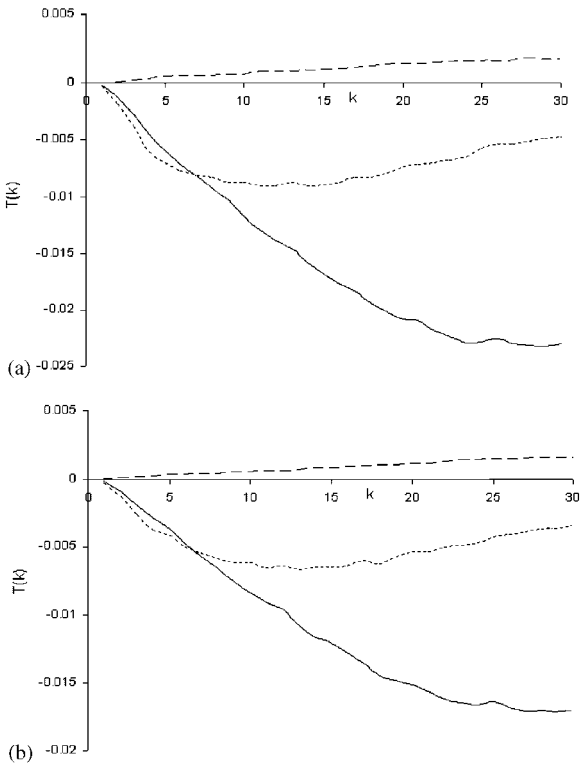

Figure 4. Energy transfer spectra for 64^3 grid case at: (a) $t = 1.53$; and (b) $t = 2.7$ obtained from: ——: eddy term; - - - -: modified Leonard's term; — · —: backscatter term.

models provide a steeper power law spectrum than Kolmogrov's. The best fit seems to be $(\propto)k^{-m}$ where $m = 1.95$ for SM and 1.9 for both MM and AM, as shown in Figure 6 for the AM cases.

6. TURBULENT CHANNEL FLOW SIMULATION

In this section the AM is applied to the plane channel flow simulation at three Reynolds numbers (Re_τ: based on friction velocity and half channel width) 180, 395 and 590 referred to as cases I, II and III, respectively. The domain sizes in the streamwise, wall normal and spanwise directions are $(4\pi \times 2 \times 4\pi/3)$ for case I and $(2\pi \times 2 \times \pi)$ for cases II and III. The domain lengths considered in the simulations are same as those of the DNS [22] which ensures that the streamwise and spanwise turbulence fluctuations remain uncorrelated along these homogeneous directions. For low Reynolds number case results have been compared with those of Smagorinsky (SM) and dynamic (DSM) models. Simulation without any turbulence model has also been performed (NM) to emphasize the effect of turbulence modelling. For higher Reynolds number cases results are compared only with DSM. Simulation on finer grid are also performed for the simulation using AM (referred to as AM^b) to study the grid refinement effect. The

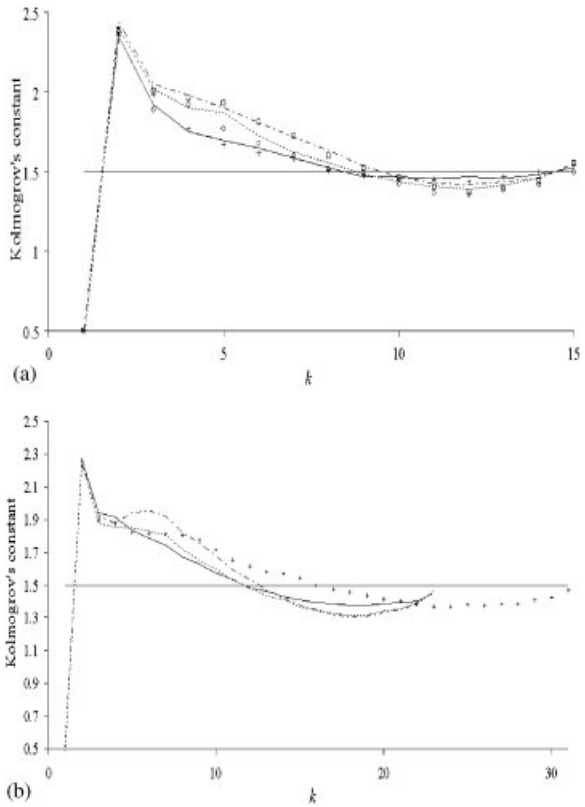

Figure 5. Kolmogrov's constant for: (a) 32^3 grid; and (b) 48^3 and 64^3 grid cases. - - - -: SM ($\varepsilon = 0.1$); $\circ$: SM ($\varepsilon = 0.2$); —·—: MM ($\varepsilon = 0.1$); $\square$: MM ($\varepsilon = 0.2$); ——— and $\times$: AM ($\varepsilon = 0.1$); $+$: AM ($\varepsilon = 0.2$).

parameters for the simulations are presented in Table IV. The numerical resolution sufficient to capture the near-wall streaks or burst ($\Delta_x^+ < 80$, $\Delta_z^+ < 30$ and $\Delta_y^+ < 2$: for the first grid cell) [34], is satisfied in all the simulations and is also comparable to other LES available in References [3, 35, 36].

The governing equations are solved using Fourier–Galerkin method in the homogeneous streamwise and spanwise directions, and second-order finite difference scheme in the wall-normal direction. Time advancement is performed using the fractional step method. A modified third-order Runge–Kutta step is used for explicit terms, and second-order Crank–Nicholson scheme for the implicit terms. The nonlinear terms in the SGSs are treated explicitly. Computations are performed on a rectangular staggered grid which is uniform in the spanwise and streamwise directions and hyperbolically stretched along the wall-normal direction. The aliasing error, along homogeneous directions, is removed using the 3/2 rule. The channel flow is governed by the constant pressure gradient, which is applied as a forcing term in the governing equations chosen appropriately to balance the targeted wall shear stress [35].

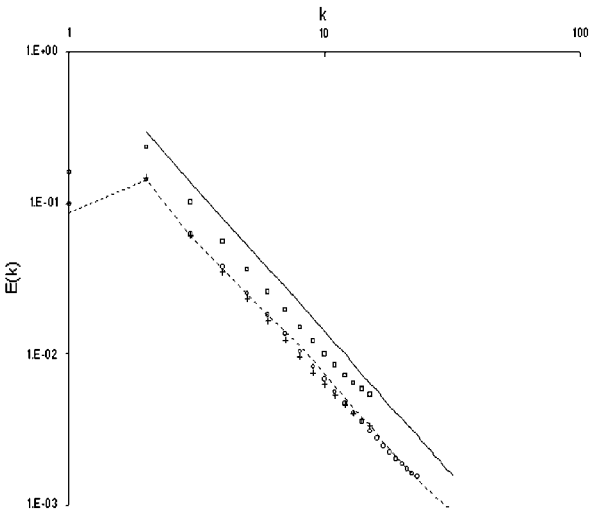

Figure 6. Energy spectrum compared with the power law for AM. ——: $k^{-1.9}$; - - - -: 64^3 grid; ○ : 48^3 grid; + : 32^3 grid ($\varepsilon = 0.1$); □ : 32^3 grid ($\varepsilon = 0.2$).

Table IV. Simulation parameters for the channel flow experiments.

Case	Model	Grid	Δ_x^+	Δ_z^+	$\Delta_{y,\min}^+$	$\Delta_{y,\max}^+$
	DNS [22]	$128 \times 129 \times 128$	17.7	5.9	—	4.4
I	NM, SM, DSM, AM[a]	$32 \times 65 \times 32$	70.68	23.56	0.63	11
	AM[b]	$48 \times 65 \times 48$	47.12	15.71	0.63	11
	DNS [22]	$256 \times 193 \times 192$	10.	6.5	—	6.5
II	DSM, AM[a]	$48 \times 73 \times 48$	51.70	25.85	1.22	20.38
	AM[b]	$64 \times 73 \times 48$	38.78	25.85	1.22	20.38
III	DNS [22]	$384 \times 257 \times 384$	9.7	4.8	—	7.2
	DSM, AM[a]	$64 \times 97 \times 64$	57.92	28.96	1.35	22.85

The model coefficients obtained in the restricted framework of the isotropic homogeneous turbulence are not capable to account for the flow inhomogeneity [36]. Thus, to account for the near-wall effect Van-Driest-type damping function [37] is used. In the simulations the filter width Δ is obtained based on the geometric average of mesh spacing in Cartesian directions $\Delta = (\Delta_x \Delta_z \Delta_y(y))^{1/3}$. Because of the inhomogeneity of the grid in the wall-normal direction the commutative property of the filtering and derivative operation does not hold, which is one of the assumption involved in deriving Equation (2). Authors acknowledge the fact that such *ad hoc* modifications are not suitable for LES simulation [5]. However, the results based on these assumptions are worth reporting and will form the basis of future improvements to the model. For the Smagorinsky model, coefficient $C_s = 0.01$ is recommended for channel flow which is used in this paper. The dynamic model coefficient evaluation of the Smagorinsky model [4] computes the coefficient $C_s\Delta^2$

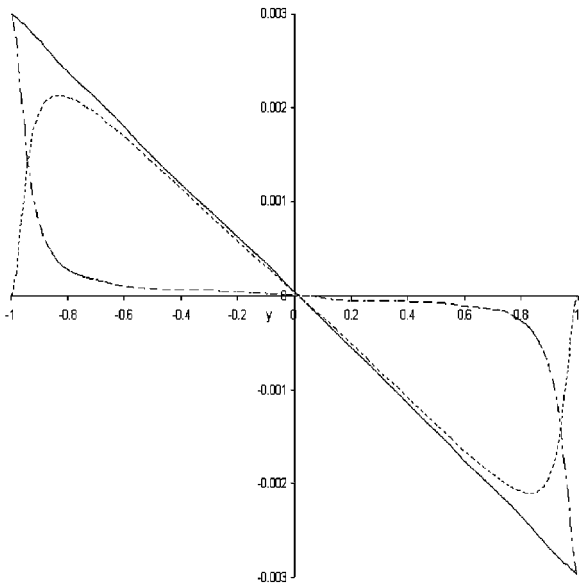

Figure 7. Profiles of shear stresses using AM^a (case I). - - -: turbulent ($\langle -u'v' \rangle + \langle \tau_{uv} \rangle$); —·—: viscous ($1/Re\langle \partial \tilde{u}/\partial y \rangle$); —: total stress (turbulent + viscous).

using explicit filtering along homogeneous directions, numerically performed using Simpson's rule [35].

The artificial initial velocity field is obtained by imposing random phase perturbations over the fully developed mean channel flow. The phases adjust themselves initially during a transient period. A statistically steady state is identified by nearly periodic nature of the wall stresses and by the straight line behaviour of the total shear stress as shown in Figure 7. To obtain a better statistical sample the running averages ($\langle . \rangle$: both plane and time averaged) of the turbulent quantities are computed after the statistically steady state is reached.

The numerical results are first presented for the mean properties, including streamwise mean velocity profile and shear stress. Accurate predictions of these quantities are necessary, but not sufficient to access the model performance as suggested by Zang [34]. Hence, the results are further interrogated for turbulence intensities and higher-order statistics. The effect of subgrid scales can be estimated for the turbulence intensities but not for higher-order statistics, thus only qualitative analysis has been performed for the latter. Finally, the dissipation, $\varepsilon = -\langle \tau_{ij} \hat{D}_{ij} \rangle$, produced by the AM is compared with other models. The capability of the AM to represent backscatter is also highlighted.

6.1. *Mean properties*

Mean skin friction coefficients obtained in all the AM and DSM simulations agree well (within 1–2%) of the target values but, SM underestimates its value considerably (about 5%) whereas the NM case overestimates by 8%. The profile of the mean streamwise velocity field has been shown in Figure 8. For case I, both the DSM and the AM^a simulations produce

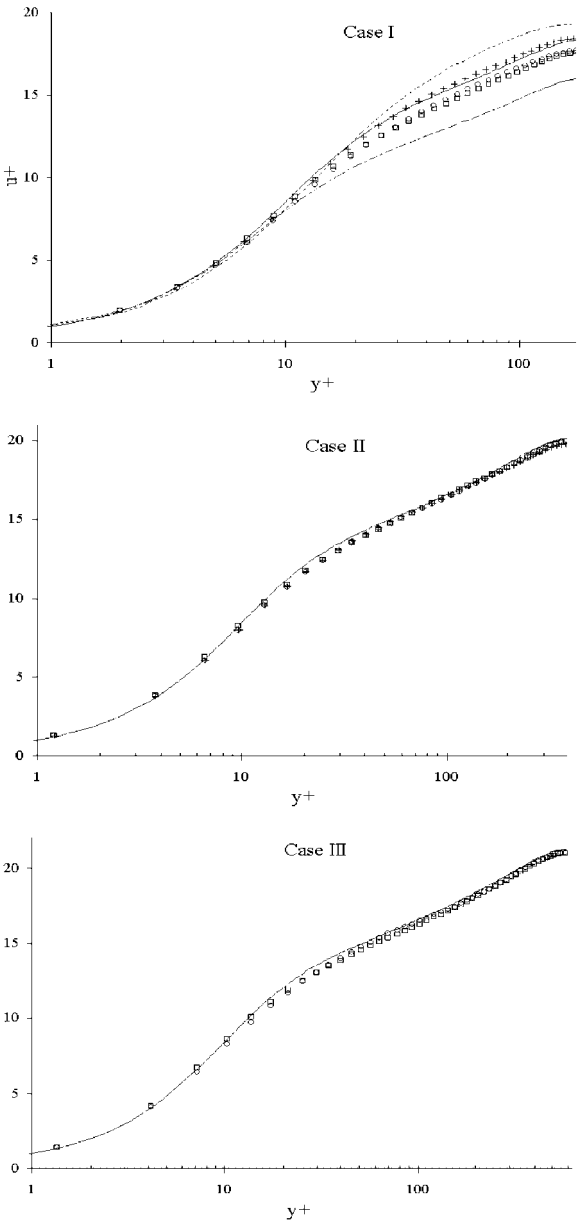

Figure 8. Mean streamwise velocity profile ($u^+ = u/u_\tau$). —-—: NM; - - - : SM; □ : DSM; ○ : AM^a; + : AM^b; — : DNS [22].

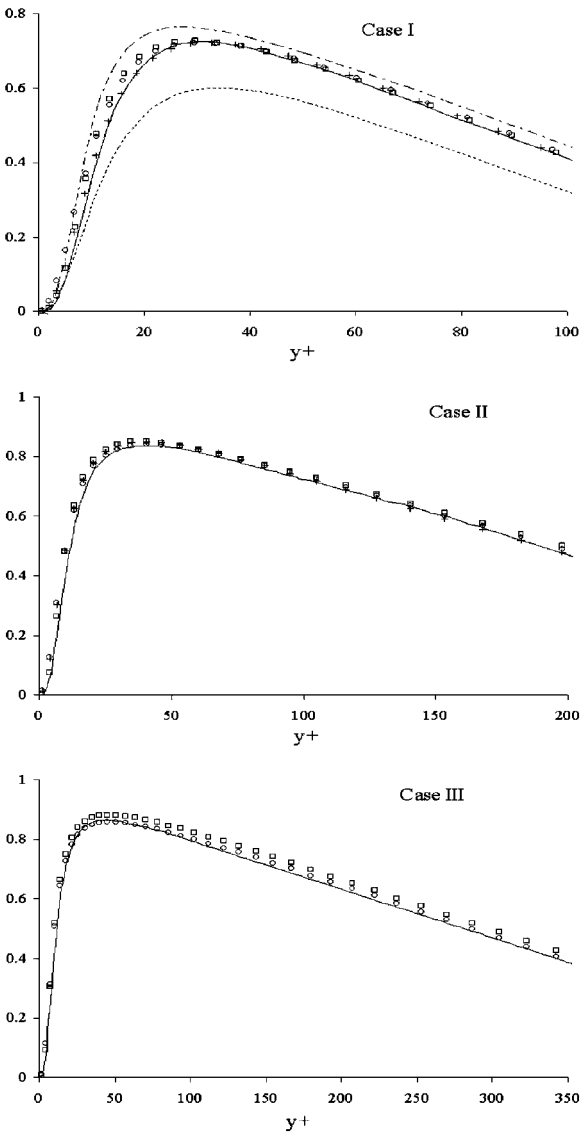

Figure 9. Reynolds stress ($\langle -u'v' \rangle + \langle \tau_{uv} \rangle$) normalized by u_τ^2 compared with DNS result. Same key as Figure 8.

good results in the sublayer, buffer layer and log layer regions. However, the Smagorinsky model deviates from the log profile and NM underpredicts the velocity profile considerably. The AM^b simulation predicts slightly lower wall stresses thereby predicting larger intercept in log layer. This profile matches exactly with the DNS data, where the larger intercept is regarded as the low Reynolds number effect [22]. In cases II and III the mean velocity profile from both the AM and DSM are in good agreement with the DNS results and grid refinement

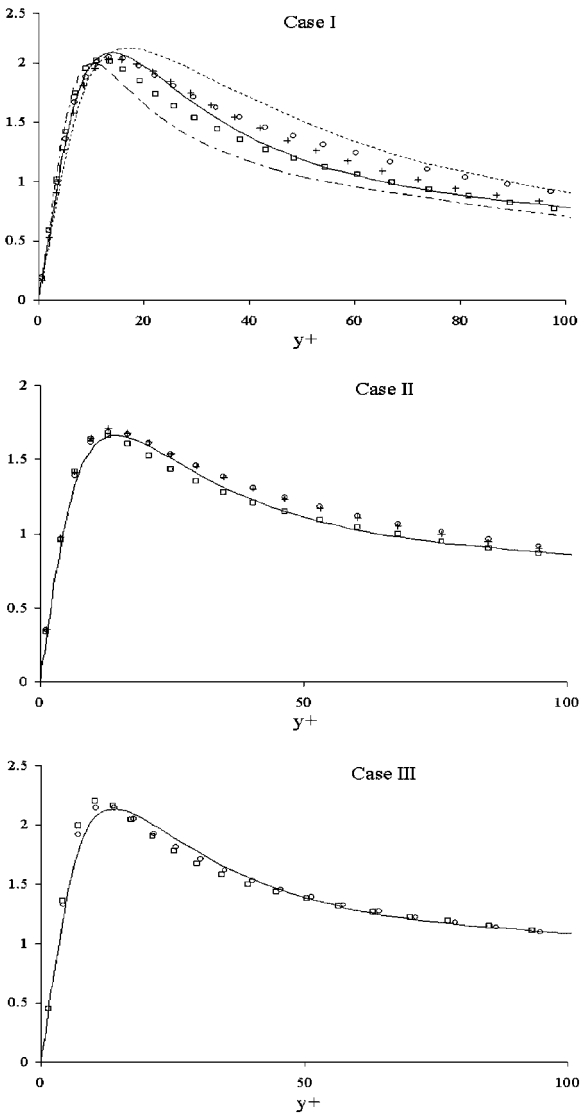

Figure 10. RMS values of streamwise velocity fluctuations (u') normalized by u_τ^2. Same key as Figure 8.

does not seem to have substantial effect. Figure 9 presents the Reynolds shear stress obtained in the numerical simulations. Again, both the AM and DSM predict the stresses in good agreement with the DNS results, whereas SM underpredicts its value and NM overpredicts its value. The fine grid simulation has the same behaviour as that of the coarse grid simulation in accordance with the observation of Zang [34]. In case III, the AM results are slightly better than that of the DSM for the shear stress.

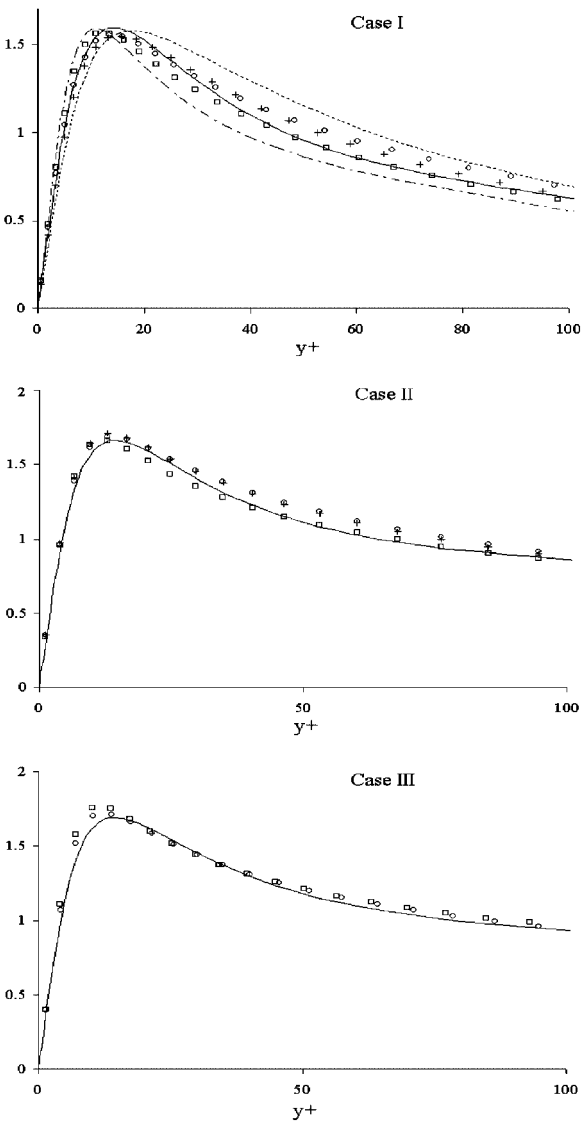

Figure 11. RMS values of wall normal velocity fluctuations (v') normalized by u_τ^2. Same key as Figure 8.

6.2. *Turbulence intensities*

Turbulence intensities from the LES calculations are compared with the DNS data by taking into account the contributions from the SGSs [17]. Figures 10–12 show the root mean square (rms) velocity fluctuation predicted by the various models. For case I, AM^a predicts the peak accurately, but deviates in the region away from the wall. On the other hand, DSM shows good agreement away from the wall but underestimates the peak. Whereas, both NM

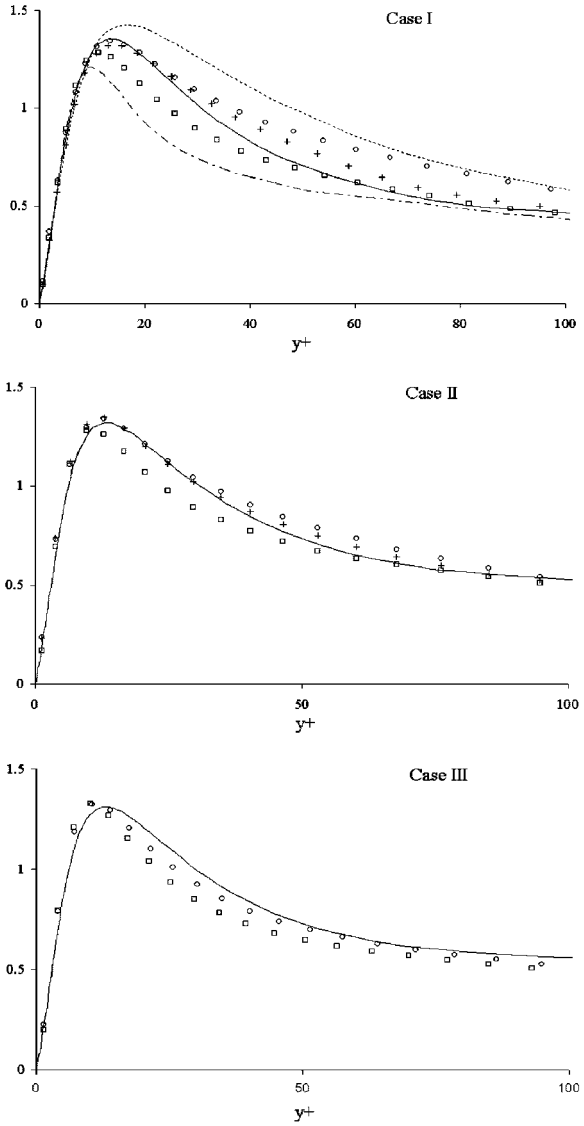

Figure 12. RMS values of spanwise velocity fluctuations (w') normalized by u_τ^2. Same key as Figure 8.

and SM results do not agree with the DNS results. The same behaviour is observed for the other velocity components too. The results on a finer grid AM^b improves the coarse grid results by predicting a better profile. For higher Reynolds number case both the AM and DSM show similar results. However, the AM predicts the streamwise component better than DSM. The AM predicts the peak of the velocity fluctuations better than DSM in the simulations.

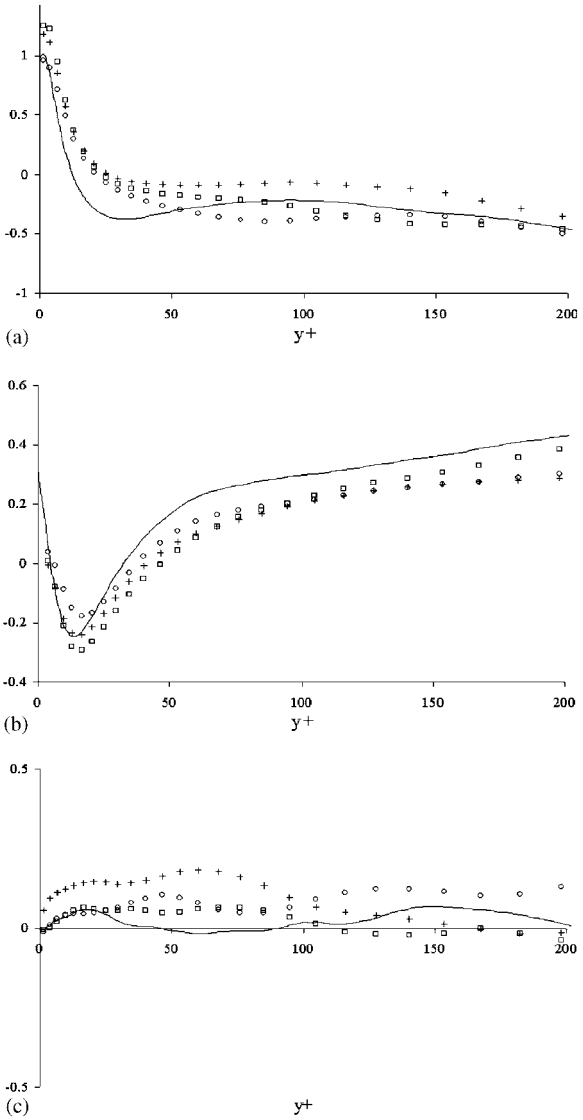

Figure 13. Skewness factor for case II: (a) $S(u')$; (b) $S(v')$; and (c) $S(w')$. Same key as Figure 8.

6.3. *Higher-order statistics*

Skewness and flatness factors are defined as (where repeated indices do not imply summation):

$$S(u'_i) = \frac{\langle u'^3_i \rangle}{\langle u'^2_i \rangle^{3/2}}, \quad F(u'_i) = \frac{\langle u'^4_i \rangle}{\langle u'^2_i \rangle^2}; \quad i = 1, 2, 3$$

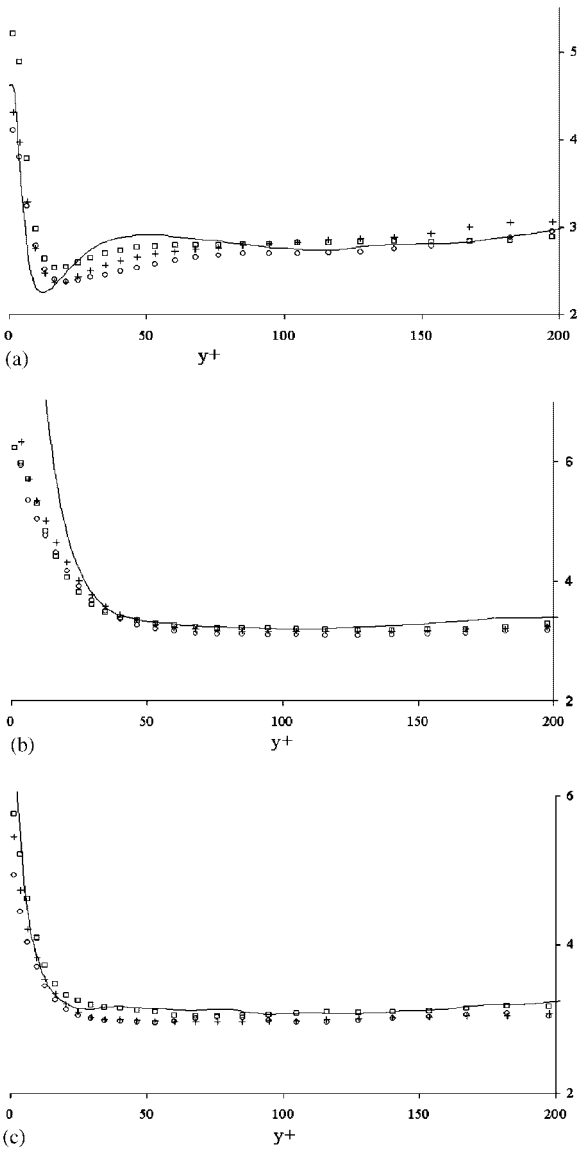

Figure 14. Flatness factor for case II: (a) $F(u')$; (b) $F(v')$; and (c) $F(w')$. Same key as Figure 8.

Comparison of these higher-order statistics of turbulent flow are considered stringent requirements for the LES modelling approach [34]. A perfect agreement of LES statistics with DNS is not expected as the subgrid contributions cannot be estimated [6], thus only the qualitative nature of the results will be discussed. Since the small scales tend to be more homogeneous and isotropic than the larger ones, their effect should be to decrease skewness. All the cases show similar qualitative behaviour, so profiles for case II are only presented in Figures 13 and 14.

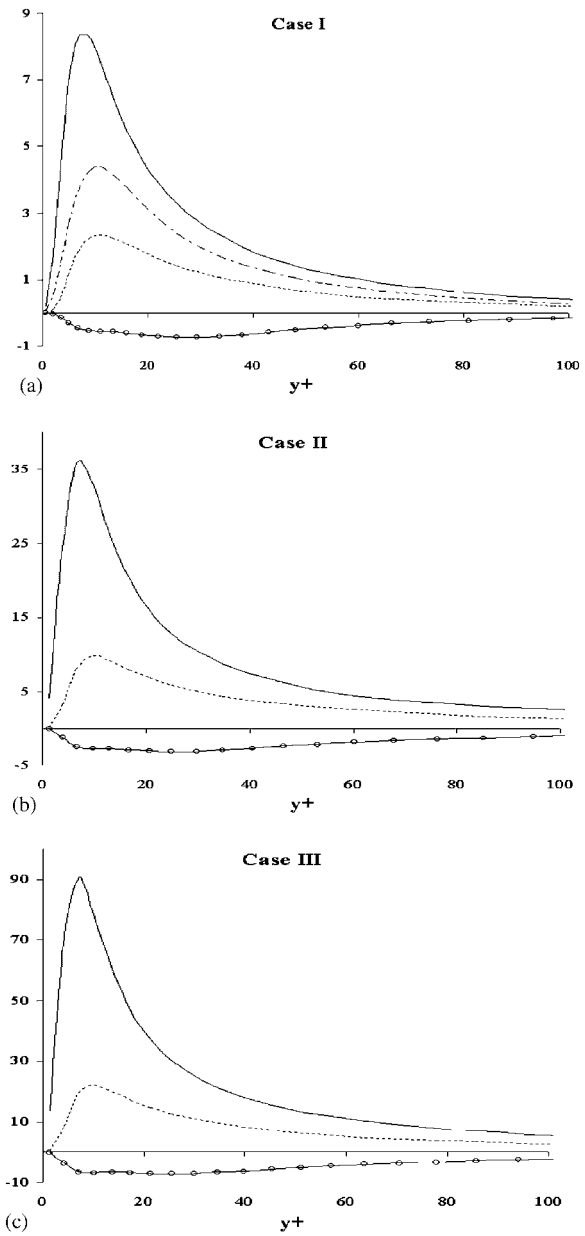

Figure 15. Plane average subgrid dissipation: (a) case I; (b) case II; and (c) case III. —·— : SM; - - -: DSM; — : AM^a; –○– : backscatter using AM^a.

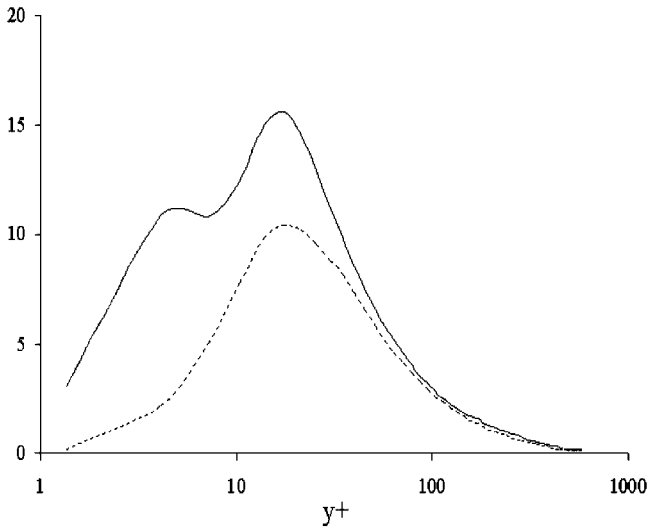

Figure 16. Plane average isotropic subgrid dissipation for case III. - - - : DSM; — : AM^a.

DNS results show that $S(u')$ is positive near the wall and negative away from the wall, due to the interaction of high-speed flow away from the wall and the low-speed flow near the wall. This behaviour of $S(u')$ is captured by all the models. The positive region is overpredicted in all the simulations, most by SM and least by AM. The results on a finer grid, AM^b, exhibit the best profile. Due to the presence of strong negative v' motion [38] in the buffer region, $S(v')$ is negative locally, as seen in all the simulations. The simulation using AM predicts the negative peak better than both the SM and DSM. Prediction of the width of the negative skewness region is best for AM and worst for SM. $S(w')$ should be zero because of the flow symmetry along the spanwise direction [6]. The results in all of the simulations vary but stay close to this value. The AM provides better qualitative results, followed by DSM and SM.

At the wall the turbulence is highly intermittent leading to large flatness. Since the effect of SGS motion is to increase these values numerical results should underpredict the values. Both the DSM and SM overpredicts the value of $F(u')$ near the wall, whereas the AM performs much better. For the other two components, $F(v')$ and $F(w')$, both AM and DSM fail to predict higher values at the wall and show similar behaviour, this may be due to substantial contribution of SGS motion near the wall. In the region away from the wall the flatness values converge to 3, which correspond to the value of a Gaussian distribution. The grid refinement improves the profile in case I, but not much in case II.

6.4. SGS dissipation

As seen in Figure 15, the nonlinear model provides backscatter independently via the fourth term on the RHS of Equation (12). The amount of backscatter is slightly less than that

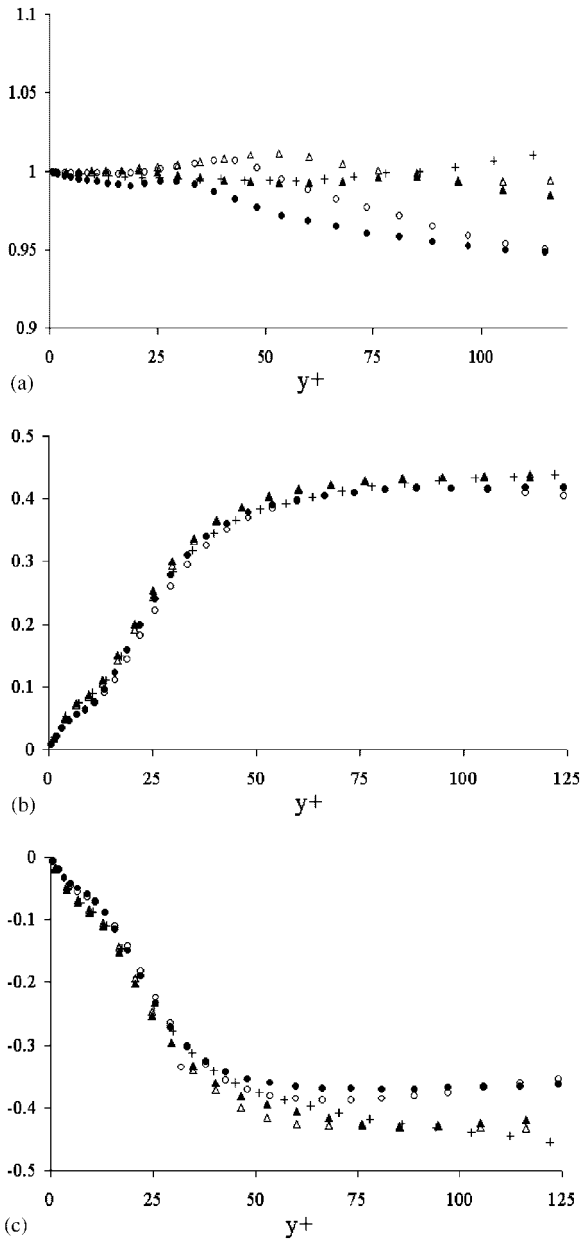

Figure 17. The subgrid dissipation provided by three terms of algebraic model (12): (a) c_f; (b) c_L; and (c) c_b. ○ : case I; △ : case II; + : case III; SOLIDS: AM^b.

obtained by Terracol and Sagaut [36] and peaks at $y+ = 30$ as compared to $y+ = 12$ predicted from *a priori* analysis [6]. The reason for this might be the use of *ad hoc* damping function. Near the wall, eddy viscosity term in the AM dominates over the other two terms and produces most of the dissipation, whereas the modified Leonard's term produces forward scatter nearly equal to the backscatter, which is about 40% of the net dissipation. The net forward scatter of energy produced by the AM agrees qualitatively with the other models and predicts the peaks correctly at about $y+ = 12$ [6]. However, AM is clearly the most dissipative and produces twice the dissipation as that of SM and about four times than that of the DSM. The dissipation produced by AM is comparable to that other numerical results [36, 37]. Further analysis of the energy transfer between resolved and subgrid scale motion is possible by separating SGS dissipation into the inhomogeneous component ($\varepsilon_{\text{inh}} = -\langle\tau_{ij}\rangle\langle\hat{D}_{ij}\rangle$) and the isotropic component ($\varepsilon_{\text{iso}} = \varepsilon - \varepsilon_{\text{inh}}$) [7]. The inhomogeneous part represents the enhancement of SGS turbulence in the presence of mean-flow gradients and is non-negative throughout the channel, which is depicted by all the models. Whereas, in *a priori* analysis the isotropic part shows a complicated nature and exhibit negative value in the buffer layer region [7]. Although the negative values are not obtained by any of the models, the AM does give a pronounced kink in the sublayer region as shown in Figure 16. Prediction of higher backscatter in the buffer layer would have resulted in the negative values. Figure 17 displays the energy transfer coefficient by the AM terms (12). The energy transfer coefficients for all the simulations shows similar nature with values converging to a constant away from the wall, which is different from the values in isotropic cases based on which model coefficients were computed. However, the independence of the energy transfer characteristic of the model terms over the range of Reynolds number suggests that these terms can be utilized to predict backscatter accurately by adjusting the model coefficients, as addressed in the conclusions.

7. CONCLUSIONS

The algebraic model proposed in this paper is obtained from the second-order approximation of the subgrid stress constitutive equation. The model thus obtained has an additional term over the mixed model, which provides distinct modelling of the backscatter of energy. The unknown model coefficients are computed for the canonical case such as to produce appropriate amount of dissipation through modified Leonard's, cross and Reynolds' terms. In *a posteriori* analysis the energy transfer coefficients of the model terms are in close agreement with the canonical case, thus the model terms perform as expected. For the isotropic decaying turbulence AM is found to be less dissipative than the SM, this is due to the explicit backscatter term which leads to more energy in the higher wavenumber range, thereby overpredicting the total resolved scale kinetic energy. Although SM provides better approximation of the overall dissipation, the energy transfer capability of the AM is better than both the MM and the SM, and has a wider inertial subrange. In the forced isotropic case AM performs better than both the SM and MM in predicting Kolmogrov's constant. The results of AM is a slight improvement over the MM for isotropic turbulence cases, but the addition of the backscatter term vastly improves the capability of the model to reproduce the normal stress anisotropy, as is evident from the results of the homogeneous *plane shear* and *plane strain* flows.

To test the ability of the model to predict the near-wall turbulent structures, turbulent plane channel simulations were performed over a range of Reynolds number ($Re_\tau = 180, 395, 590$). The predictions of the AM have been compared with dynamic model, Smagorinsky model and the DNS data. Both the algebraic and dynamic models predict the mean flow quantities better than the Smagorinsky model. The AM provides better prediction of the turbulence intensities than the dynamic model. The results on finer grid using AM for $Re_\tau = 180$ is able to predict the exact DNS velocity profile, regarded as the low Reynolds number effect. Qualitative analysis of the higher-order statistics, skewness and flatness, show that both the dynamic and algebraic models capture the nature of the profile. However, the results of the AM are closer to the DNS data than the dynamic model. Results show that the AM is more dissipative than the Smagorinsky and dynamic models. This is due to the higher value of the eddy viscosity coefficient. Capability of the model in producing backscatter independently via the modelled backscatter term is also evident. The model predicts a kink in the isotropic dissipation profile, but fails to predict a negative value in the buffer layer. This is due to the use of a damping function in the near-wall region, which restricts the maximum backscatter to occur in the buffer layer. The AM is based only on first-order derivative term and has constant model coefficients, so the computation of stresses in numerically inexpensive. Estimate of the CPU time show that AM requires $\sim$3% more time than SM, whereas dynamic modelling approach is $\sim$12% more expensive.

The numerical results suggest a better estimate of the model coefficients are still required for the model. The model coefficients computed in the framework of isotropic turbulence cannot be extended to near-wall flows thus model coefficient cannot be predicted accurately, *a priori*, for the model. However, the dynamic model coefficient evaluation will make the model sensitive to the local state of the flow and suitable for more complex simulations. Further, the cross terms are modelled along with the Reynolds stresses and their characterization is still a challenge for SGS modelling.

APPENDIX A: ALGEBRAIC STRESS CLOSURE

Taking the divergence of the governing equations, the Poisson's equation of the pressure can be obtained. The integral solution of the Poisson's equation using Green's theorem yields [25],

$$Q_{ij} = \frac{1}{2\pi} \int_\Omega \left[\lambda \left(\left.\frac{\partial u_m}{\partial x_n}\right|_\xi , \left.\frac{\partial u_n}{\partial x_m}\right|_\xi , \left.\frac{\partial u_i}{\partial x_j}\right|_{\mathbf{x}} \right) + 2 \left.\frac{\partial \hat{u}_m}{\partial x_n}\right|_\xi \lambda \left(\left.\frac{\partial u_n}{\partial x_m}\right|_\xi , \left.\frac{\partial u_i}{\partial x_j}\right|_{\mathbf{x}} \right) \right] \frac{1}{r} \, \mathrm{d}\Omega(\boldsymbol{\xi}) + \chi_{ij}$$

where the first term in the integral is the contribution from the sugrid terms only (*return term*), whereas the second term depends explicitly on the gradient of resolved velocity field (*rapid term*). The last term involves integral over the surface of domain Ω and is called the *wall term*. These terms are modelled as a functional of resolved scale following Launder (cf. Reference [25], neglecting the wall term) such that,

$$Q_{ij} = 3c_1 \frac{\varepsilon}{K_{\mathrm{sgs}}} \left(\frac{2}{3} K_{\mathrm{sgs}} \delta_{ij} - \tau_{ij} \right) + \alpha \left(\frac{2}{3} P \delta_{ij} - P_{ij} \right) + \beta \left(\frac{2}{3} P \delta_{ij} - \Delta_{ij} \right) - \gamma K_{\mathrm{sgs}} \tilde{D}_{ij}$$

Here, c_1, α, β and γ are constants and

$$\tilde{D}_{ij} = \frac{1}{2}\left[\frac{\partial \tilde{u}_i}{\partial x_j} + \frac{\partial \tilde{u}_j}{\partial x_i}\right] \quad \text{and} \quad \Delta_{ij} = -\left(\tau_{ik}\frac{\partial \tilde{u}_k}{\partial x_j} + \tau_{jk}\frac{\partial \tilde{u}_k}{\partial x_i}\right)$$

Similarly, the diffusion term F_{ij} are expressed in terms of subgrid correlation (cf. Reference [25]) as

$$F_{ij} = C\frac{\partial}{\partial x_k}\left[\frac{K_{\text{sgs}}}{\varepsilon}\left(\lambda(u_k,u_l)\frac{\partial\lambda(u_i,u_j)}{\partial x_l} + \lambda(u_j,u_l)\frac{\partial\lambda(u_k,u_i)}{\partial x_l} + \lambda(u_i,u_l)\frac{\partial\lambda(u_j,u_k)}{\partial x_l}\right)\right]$$

Further, neglecting the last two terms on RHS (cf. Reference [25] for discussion) yields,

$$F_{ij} = T_{ij}D$$

This assumption leads to the simplified form of the algebraic stress closure Equation (9). Lastly, the dissipation term is modelled in isotropic form, i.e.

$$\varepsilon_{ij} = \tfrac{2}{3}\varepsilon\delta_{ij}$$

The other assumption involved in obtaining Equation (9) is that the derivative of T_{ij} is vanishingly small [25] which is based on the structural equilibrium.

APPENDIX B: CANONICAL FLOWS

For homogeneous isotropic turbulence the general fourth- and sixth-order tensors yields [8] (where $\langle . \rangle$ implies emsemble average),

$$\begin{aligned}
\langle \tilde{D}_{ij}\tilde{D}_{ij}\rangle &= \frac{30}{4}\left\langle\left(\frac{\partial \tilde{u}_1}{\partial x_1}\right)^2\right\rangle \\
\left\langle \frac{\partial \tilde{u}_i}{\partial x_k}\frac{\partial \tilde{u}_j}{\partial x_k}\tilde{D}_{ij}\right\rangle &= \frac{35}{2}\left\langle\left(\frac{\partial \tilde{u}_1}{\partial x_1}\right)^3\right\rangle \\
\left\langle \frac{\partial \tilde{u}_k}{\partial x_i}\frac{\partial \tilde{u}_k}{\partial x_j}\tilde{D}_{ij}\right\rangle &= \frac{35}{2}\left\langle\left(\frac{\partial \tilde{u}_1}{\partial x_1}\right)^3\right\rangle
\end{aligned} \tag{B1}$$

Estimation of the above quantities requires the following integral, obtained assuming an infinite inertial subrange with Kolmogrov's energy spectrum [2, 15].

$$\begin{aligned}
\tilde{E}(k) &= |\dot{G}(k)|^2 C_k \varepsilon^{2/3} k^{-5/3} \\
\left\langle\left(\frac{\partial \tilde{u}_1}{\partial x_1}\right)^2\right\rangle &= \frac{2}{15}\int_0^\infty k^2\tilde{E}(k)\,\mathrm{d}k = \frac{12^{2/3}}{\Delta^{4/3}}\left[\Gamma\left(\frac{5}{3}\right)\frac{C_k}{10}\right]\varepsilon^{2/3} \\
\left\langle\left(\frac{\partial \tilde{u}_1}{\partial x_1}\right)^3\right\rangle &= -S_k\left\langle\left(\frac{\partial \tilde{u}_1}{\partial x_1}\right)^2\right\rangle^{3/2}
\end{aligned} \tag{B2}$$

where $|\grave{G}(k)| = e^{-\Delta^2 k^2/24}$ for Gaussian filter and $\Gamma(.)$ is the gamma function. The results in this paper are obtained using appropriate values of the skewness factor ($S_k = 0.4$) and Kolmogrov's constant ($C_k = 1.62$).

REFERENCES

1. Leslie DC, Quarini GL. The application of turbulence theory to the formulation of subgrid modelling procedures. *Journal of Fluid Mechanics* 1979; **91**:65–91.
2. Pope SB. *Turbulent Flows*. Cambridge University Press: Cambridge, MA, 2000.
3. Domaradzki JA, Saiki EM. A subgrid-scale model based on the estimation of unresolved scales of turbulence. *Physics of Fluids A* 1997; **9**(7):2148–2164.
4. Lilly DK. A proposed modification of the Germano subgrid-scale closure method. *Physics of Fluids A* 1992; **4**(3):633–634.
5. Sagaut P. *Large Eddy Simulation for Incompressible Flows*. Springer: Berlin, 2002.
6. Piomelli U. High Reynolds number calculations using the dynamic subgrid scale stress model. *Physics of Fluids A* 1993; **5**(6):1484–1490.
7. Hartel C, Kleiser L. Analysis and modeling of subgrid-scale motions in near-wall turbulence. *Journal of Fluid Mechanics* 1998; **356**:327–335.
8. Kosovic B. Subgrid scale modeling for the large-eddy simulation of high-Reynolds-number boundary layer. *Journal of Fluid Mechanics* 1997; **336**:151–182.
9. Horiuti K. A new dynamic two-parameter mixed model for large-eddy simulation. *Physics of Fluids* 1997; **9**(11):3443–3464.
10. Chasnov JR. Simulation of the Kolmogorov inertial subrange using an improved subgrid model. *Physics of Fluids* 1991; **3**(1):188–200.
11. Carati D, Ghosal S, Moin P. On the representation of backscatter in dynamic localization models. *Physics of Fluids A* 1995; **7**(3):606–616.
12. Schumann U. Stochastic backscatter of turbulence energy and scalar variance by random subgrid-scale fluxes. *Proceedings of the Royal Society of London, A* 1995; **451**:293–318.
13. Piomelli U, Yu Y. Subgrid-scale energy transfer and near-wall turbulence structure. *Physics of Fluids A* 1996; **8**(1):215–224.
14. Domaradzki JA, Adams NA. Direct modeling of subgrid scales of turbulence in large eddy simulation. *Journal of Turbulence* 2002; **3**:1–19.
15. Leonard A. Energy cascade in large-eddy simulations of turbulent fluid flows. *Advanced Geophysics* 1974; **18**:237–248.
16. Liu S, Meneveau C, Katz J. Evolution and modeling of subgrid scales during rapid straining of turbulence. *Journal of Fluid Mechanics* 1999; **387**:281–320.
17. Iliescu T, Fischer PF. Large eddy simulation of turbulent channel flows by rational large eddy simulation model. *Physics of Fluids* 2003; **15**(10):3036–3047.
18. Meneveau C, Katz J. Scale-invariance and turbulence models for large-eddy simulations. *Annual Review of Fluid Mechanics* 2000; **32**:1–32.
19. Carati D, Winckelmans GS, Jeanmart H. On the modeling of the subgrid-scale and filtered-scale stress tensors in large-eddy simulation. *Journal of Fluid Mechanics* 2001; **441**:119–138.
20. Sarghini F, Piomelli U, Balaras E. Scale-similar models for large eddy simulations. *Physics of Fluids A* 1999; **11**(6):1596–1607.
21. Lesieur M. *Turbulence in Fluids* (2nd edn). Kluwer: Dordrecht, 1993.
22. Moser RD, Kim J, Mansour NN. Direct numerical simulation of turbulent channel flow up to $Re_\tau = 590$. *Physics of Fluids* 1999; **11**(4):943–945.
23. Germano M. A proposal for a redefinition of the turbulent stresses in the filtered Navier–Stokes equations. *Physics of Fluids A* 1986; **29**(7):2323–2324.
24. Bhushan S. Development of a nonlinear model for subgrid scale turbulence and its applications. *Ph.D. Dissertation*, Mississippi State University, 2003.
25. Warsi ZUA. *Fluid Dynamics*, *Theoretical and Computational Approach* (2nd edn). CRC Press: Boca Raton, FL, 1998.
26. Galperin B, Orszag SA. *Large Eddy Simulation of Complex Engineering and Geophysical Flows*. Cambridge University Press: Cambridge, MA, 1993.
27. Mohseni K, Kosovic B, Shkoller S, Marsden JE. Numerical simulations of Lagrangian averaged Navier–Stokes equations for homogeneous isotropic turbulence. *Physics of Fluids A* 2003; **15**(2):524–544.
28. Brun C, Friedrich R. Modeling the test SGS tensor T_{ij}: an issue in the dynamic approach. *Physics of Fluids A* 2001; **13**(8):2373–2385.
29. Hinze JO. *Turbulence*: *An Introduction to its Mechanism and Theory*. McGraw-Hill: New York, NY, 1959.

30. Schilling O, Zhou Y. Analysis of spectral eddy viscosity and backscatter in incompressible, isotropic turbulence using statistical closure theory. *Physics of Fluids A* 2002; **14**(3):1244–1258.
31. Canuto VM, Cheng Y. Determination of the Smagorinsky–Lilly constant C_s. *Physics of Fluids A* 1997; **9**(5):1368–1378.
32. Collis SS. *Multiscale Methods for Turbulence Simulation and Control*. Lecture Notes, 2002.
33. Stefano GS, Vasilyev OV. Sharp cutoff versus smooth filtering in large eddy simulation. *Physics of Fluids A* 2002; **14**(1):362–369.
34. Zang TA. Numerical simulation of the dynamics of turbulent boundary layers: perspectives of a transition simulator. *Philosophical Transactions of the Royal Society of London Series A* 1991; **336**:95–102.
35. Chang Y. Approximate models for optimal control of turbulent channel flow. *Ph.D. Dissertation*, Mississippi State University, 2000.
36. Terracol M, Sagaut P. Multilevel-based dynamic approach for subgrid-scale modeling in large eddy simulation. *Physics of Fluids* 2003; **15**(12):3671–3682.
37. Winckelmans GS, Wray AA, Vasilyev OV, Jeanmart H. Explicit-filtering large-eddy simulation using the tensor-diffusivity model supplemented by a dynamic Samgorinsky term. *Physics of Fluids* 2001; **5**(13):1385–1403.
38. Kim J, Moin P, Moser R. Turbulence statistics in fully developed channel flow at low Reynolds number. *Journal of Fluid Mechanics* 1987; **177**:133–165.

